CHEMISTRY OF MATERIALS

pubs.acs.org/cm

Article

Toward Atomistic Understanding of Materials with the Conversion−Alloying Mechanism in Li-Ion Batteries

Heesoo Park,* Adri C. T. van Duin, and Alexey Y. Koposov*

Cite This: *Chem. Mater.* 2023, 35, 2835−2845

Read Online

ACCESS | Metrics & More | Article Recommendations | Supporting Information

ABSTRACT: The need for practical anodes for rechargeable batteries calls for new materials with improved storage capacity and cycling stability compared to the materials of today. Materials capable of alloying with alkali metals have been long viewed as a promising pathway to address this challenge. Meanwhile, severe drawbacks associated with the use of such materials led to the development of suitable alternatives, in which governing the reaction mechanism in a battery combines conversion and alloying reactions. These materials feature a high storage capacity and long-term stability during electrochemical cycling. However, the development of these materials is impeded by a lack of fundamental structural understanding due to the complexity of the chemical transformations taking place during battery cycling. Furthermore, amorphization, which is prevalent in these materials, also severely limits the conventional methods of characterization. In the present work, we propose a computational methodology for understanding the structure and reaction mechanism of these conversion−alloying materials by using amorphous substoichiometric silicon nitride as a model system. The developed ReaxFF parameter set allowed exploring the atomistic structure of this material and verify the resulting models through a comparison of calculated and experimentally obtained pair distribution functions (PDFs). The developed methodology also allowed exploring the structural changes occurring during lithiation and delithiation, i.e., operation mechanism in a battery. The analysis of the atomistic structure demonstrates that initial lithiation results in the formation of a Si network, which later participates in further lithiation process. Delithiation also influences the evolution of the amorphous Si network facilitating separation of nitrogen-rich and Si-rich regions and, therefore, confirming the conversion mechanism proposed earlier. Furthermore, the proposed approach allows modeling not only changes at the atomistic scale but also predicting the experimental PDF at different stages of cycling which allows experimentally verifying the outcome of modeling.

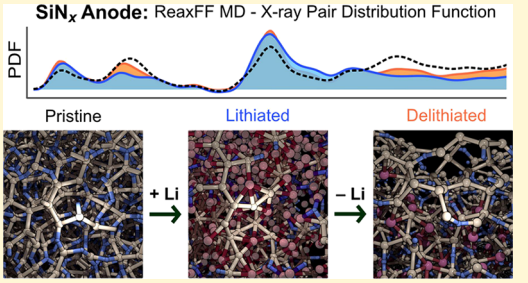

1. INTRODUCTION

The goal to improve the performance of modern rechargeable batteries stimulated tremendous interest in the development of materials. However, further advancements are limited by the materials set used today.[1] This particularly applies to the most developed Li-ion batteries (LIBs), and among various components of LIBs, anode active materials have been viewed as one of the platforms for improvements. In particular, the currently used anode material, graphite, caps the lithiation capacity at 372 mAh/g as graphite accommodates Li atoms intercalated between the graphene layers, forming LiC_6 as a final product of lithiation.[2,3] This capacity limit of graphite greatly contrasts with high theoretical lithiation capacity, which could be achieved by use of the materials operating under the alloying mechanism. Silicon (Si) with its theoretical capacity of 3579 mAh/g (originating from the formation of the $Li_{15}Si_4$ alloy as a final product of lithiation) represents the most well-studied example of alloying materials.[4] A combination of high specific capacity of Si-based anodes and a low operation voltage (0.2−0.4 V vs Li^+/Li) provides a possibility to drastically improve the specific energy storage capacity of modern LIBs.[5]

Despite their potential benefits, the implementation of Si-based and similar alloying anode materials is severely limited due to the low stability of these materials upon cycling. The large lithium storage capacity of alloying materials (Si, Sn, and others) causes significant volumetric changes of the active particles during lithiation and delithiation, promoting several failure mechanisms.[3,4,6,7] Among various promising strategies to mitigate these degradation paths, a family of materials undergoing the combined conversion and alloying mechanism (i.e., conversion−alloying materials; CAMs) represent a promising solution to deliver stable long cycle life while maintaining high specific capacities.

CAMs were designed to alleviate the issues associated with the volumetric changes through the cluster (or nanoparticle)

Received: December 2, 2022
Revised: February 11, 2023
Published: February 23, 2023

formation of active alloying elements embedded in the equilibrated alkali-metal anion compound of conversion elements (matrix).[5,8−10] For example, in an MX material, where M is a semimetal or metal element, such as Si, Ge, Sn, P, Sb, and Bi and X is a nonmetal element, such as N, O, S, Se, Te, the initial lithiation occurs through a conversion reaction, resulting in amorphous Li_xX. The function of the Li_xX is to buffer the volume changes of the Si clusters, and this nonequilibrium Si phase further adopts an alloying mechanism. Through further cycling, the chemical reversibility of the Li_xX and Li−Si alloying phase is the key to the overall cycling stability of the CAMs and its formation and (or) chemical composition cannot be understood without characterization of the chemical mechanism taking place during lithiation/delithiation. The characterization of such a reaction mechanism in the mixed-phase particles has been challenging because the majority of the formed products are typically amorphous, and, therefore, the mechanistic studies of the conversion process have been primarily performed using indirect electrochemical characterization.[4,11,12] Therefore, a detailed atomistic understanding of the reaction mechanism is necessary for the rational design of the new CAMs.

Substoichiometric silicon nitride (SiN_x) is a representative of CAMs experimentally shown to have a stable cycling performance.[8,13,14] In particular, Ulvestad et al. reported the cycling stability over more than 1000 lithiation/delithiation cycles, confirming the limited morphological changes through microscopy.[14] Furthermore, the reported pair distribution function (PDF) analysis demonstrated that the atomistic structure of SiN_x changes during the first cycle of SiN_x, partially confirming the proposed mechanism of conversion. The PDF technique is indispensable for characterizing amorphous (nano)materials,[15,16] such as SiN_x nanoparticles as shown by Ulvestad et al.[14] However, the interpretation of the PDF data is challenging, limiting the understanding of the phase transitions, when the material undergoes various chemical transformations during lithiation/delithiation. During these processes, such material's structural and chemical features are defined in a thermodynamical nonequilibrium state. Therefore, its characterization (based only on PDF) is challenging to represent the role of local structural relaxation at the nanoscale, when multiple phases are present in the (de)lithiated SiN_x material.

Earlier theoretical investigations revealed the structure of amorphous Li−Si alloys,[17−19] complementing the PDF analysis[20] and assisting general understanding. However, in the transition from alloying materials to CAMs (i.e., from Si to SiN_x), the reaction mechanism and structural changes are no longer analogous to the conventional Li−Si alloying mechanism. Therefore, this work is motivated to fill this gap and illustrate the methodology for atomic understanding of conversion mechanism in CAMs using SiN_x as a model structure. The main objective of this study is to provide a complementary description of the experimental PDFs unraveling the various stages in structural transformation during the lithiation and delithiation processes.

Recently developed ReaxFF MD simulations compare the structural profiles from molecular dynamics (MD) and experimental characterization techniques, because the simulated structural features corresponding to the experimentally measured scales can represent the chemical events during the structural reorganizations.[21,22] Thus, in this work, the ReaxFF parameter set was developed to successfully predict the atomistic structure transformation of SiN_x anodes during the first (de)lithiation cycle at 300 K. To directly compare the experimental and simulated PDFs, the PDF simulation method accounted for the X-ray sensitivity of the constituent elements as the low scattering power of Li may result in a vaguely different peak change. The combining approach of ReaxFF and PDF simulation methods allows exploring the structural evolution in conversion−alloying reactions by validating the amorphous and multiple phases that were observed in the experimental PDFs.

2. METHODS

2.1. ReaxFF MD Simulation. ReaxFF is one of the multiscale approaches.[23] This reactive interatomic potential covers nanoscale systems by calculating the total energies even when there is breaking and formation of the chemical bonds within the system.

As the total energies are updated at every MD step, this method bridges the gap between quantum mechanics-based and empirical potential calculations. We developed the ReaxFF parameters by comparing a collection of geometries, equations of states, and cohesive energies between the ReaxFF and DFT calculations for SiN_x in lithiated and delithiated states. We used VASP[24−26] and ORCA[27,28] programs for the calculation of the training sets of properties by employing the generalized gradient approximation density functional theory (DFT) method (see the ReaxFF and DFT result comparison in Figures S1−S3 in the Supporting Information). Furthermore, we carried out the ReaxFF MD simulations using LAMMPS[29,30] and visualized the trajectories by Ovito.[31]

2.2. PDF Simulation. The present work utilized experimental PDF analysis of the SiN_x nanoparticles as a verification method for the ReaxFF development. The PDF peak intensity of an atomic pair is not only proportional to the occurrence of such pair, but also determined by the atoms' scattering power. Therefore, we obtained the simulated SiN_x PDF patterns by considering the increase of X-ray scattering amplitude with the high atomic number, using XaNSoNS.[32] When we compared the PDF intensity of atomic pairs of different element types, the different X-ray scattering sensitivity is considered. In the calculation of PDF patterns, we employed the atomic form factors created by XaNSoNS, when considering the ReaxFF-MD-generated trajectories.

Furthermore, we provide only the reduced pair distribution function (rPDF; $G(r)$), distinguishing from PDF $g(r)$, because the reduced pair distribution function is used typically in the experiment.[16,33,34] The function of rPDF $G(r)$ obtains the intensity directly from the measured total scattering function $S(Q)$ through the Fourier transformation, defined as follows:

$$G(r) = \frac{2}{\pi}\int_0^\infty Q[S(Q) - 1]\sin(Qr)\mathrm{d}Q \tag{1}$$

where Q is the magnitude of the scattering vector, r is the interatomic distance, and $S(Q)$ is the experimental coherent X-ray scattering intensity.

For the simulated PDF pattern, $G(r)$ is defined by:[15,32]

$$G(r) = 4\pi r[\rho(r) - \rho_0],$$
$$\rho(r) = \sum_{el_i=1}^{N_{el}}\sum_{el_j=el_i}^{N_{el}}\frac{f_{el_i}f_{el_j}}{f_{av}^2}\delta(r - r_{ij}), f_{av} = \sum_{el_i=1}^{N_{el}} f_{el_i}\frac{N_{el_i}^{\mathrm{total}}}{N} \tag{2}$$

where ρ_0 is the atomic number density and ρ is the atomic pair density. Considering the X-ray scattering sensitivity for chemical elements, $f_{el_i}(q_p)$ is the X-ray atomic form factor for the chemical element el_i as a function of the predefined scattering vector magnitude q_p, r_{ij} is the distance between atoms i and j, and, $N_{el_i}^{\mathrm{total}}$ is the total number of atoms of the element el_i to obtain the average scattering factor f_{av}. The oscillating pattern of reduced PDF $G(r)$ represents the probability of finding a pair of atoms with a separation distance − r in

https://doi.org/10.1021/acs.chemmater.2c03603
Chem. Mater. 2023, 35, 2835−2845

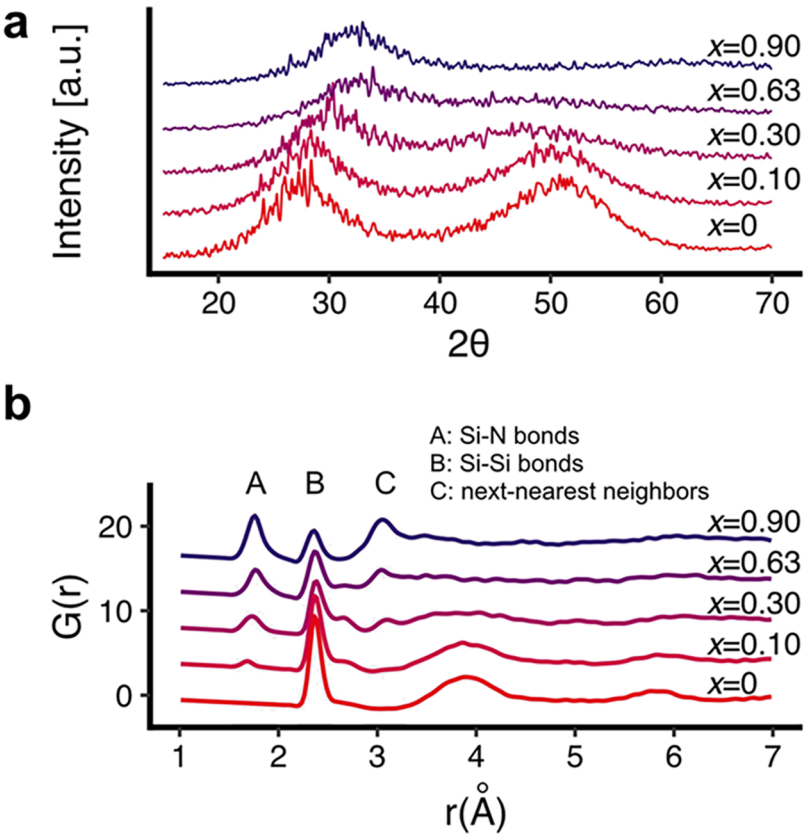

Figure 1. Simulated (a) X-ray diffraction (XRD) and (b) PDF patterns of a-SiN_x, where x = 0, 0.10, 0.30, 0.63, and 0.90.

relation to the atomic number density in the material. This definition distinguishes $G(r)$ from $g(r)$, as $g(r)$ represents a histogram of pair distances. Hence, the values of simulated $G(r)$ are comparable to the experimental characterization.

3. RESULTS AND DISCUSSION

SiN_x represents a perfect model system for the development of methodology and for understanding CAMs' mechanism during battery operation as a material experimentally demonstrated CAM's behavior and long-term cycling stability. For the present work, several compositions of SiN_x were selected with x= 0.0, 0.10, 0.30, 0.63, and 0.90: the nanoparticles of amorphous SiN_x with similar stoichiometries have been synthesized and electrochemically evaluated in the earlier work as well as characterized using the PDF.[35] Therefore, the models developed herein could be verified through a comparison of experimental and calculated PDF patterns.

Importantly, to have the simulated PDFs comparable with the experimental results, the developed ReaxFF should yield general relationships accurately between the constituent elements:

(1) The first peak of a pair in the PDF pattern is at the bond distance between two adjacent atoms. The correct equilibrium bond length established by the ReaxFF simulations enables us to determine these PDF peaks.

(2) The second peak of a pair in the PDF pattern is at the distance between the next pair of atoms. Concerning this measurement, both bond lengths and bond angles should be equal to the actual system. Then, the ReaxFF simulations deliver the correct next-nearest pair and all the other subsequent peaks.

(3) The peak intensities in the PDF represent the relative densities of pairs, while we obtain the varying coordination configurations in the atomistic structure during the ReaxFF simulations. Thus, the phase formation energy should show good agreement between the ReaxFF and DFT calculations.

Thus, we developed the ReaxFF parameter set and simulated the model structures to obtain PDFs for the several SiN_x compositions comparable between the ReaxFF simulations and the experimental results according to the criteria listed above. Thus, the ReaxFF-simulated XRD and PDF patterns of studied a-SiN_x structures were obtained from the NVT (constant volume) MD simulations as shown in Figure 1.

The nanoparticle systems consist of 5000 atoms within the periodic boundary cells. The input lattice parameters of the simulated supercells were determined, while mass densities were derived from the experimental values of the thin a-SiN_x film.[36,37] To obtain amorphous nanoparticle structures, we cooled the systems (geometries were prepared using Packmol[38]) from 1300 to 300 K in the periodic boundary condition for 40 ps (400,000 steps with the 0.1 fs time step size). This was performed for a-SiN_x with x = 0.0, 0.10, 0.30, 0.63, and 0.90, where the structure with x = 0 is equivalent to pure amorphous Si (a-Si).

For both a-Si and a-SiN_x, the XRD patterns (Figure 1a) are consistent with the experimental XRD patterns predictably demonstrating no pronounced diffraction peaks. However, the increased amount of N atoms in the structure drastically lowers the intensities of the broad peaks at 2θ = 28 and 52° as the Si−N bond formation provides an additional disorder in the Si−Si bonding network. The simulated PDF patterns showed more

https://doi.org/10.1021/acs.chemmater.2c03603
Chem. Mater. 2023, 35, 2835−2845

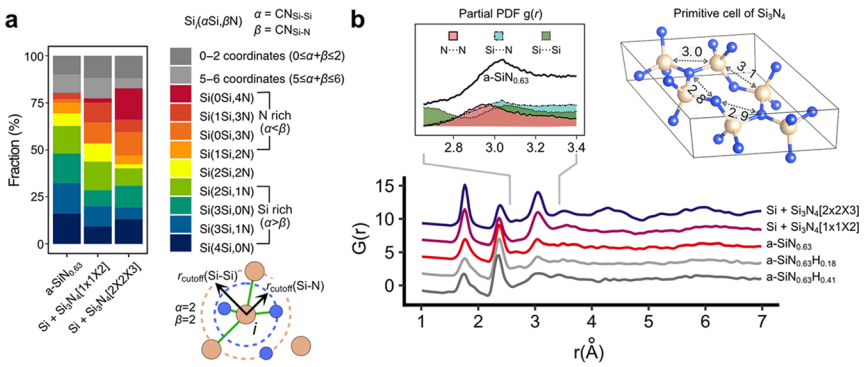

Figure 2. (a) Fraction comparisons of different coordination configurations around the Si atoms in $SiN_{0.63}$ illustrating the different local coordination for Si. The coordination sphere was defined by the distance cutoff (r_{cutoff}), and the ith Si's coordination configuration is denoted as $Si_i(\alpha Si,\beta N)$ where α and β values are the atomic coordination numbers with Si and N, respectively. (b) Simulated PDF $G(r)$ patterns of $SiN_{0.63}$ and $SiN_{0.63}$:H and the partial PDF $g(r)$ of a-$SiN_{0.63}$. Light brown and blue spheres represent Si and N, respectively. The insets above illustrate the expanded region of the partial PDFs in the range of 2.6−3.4 Å and the primitive cell of Si_3N_4 crystal structure.

pronounced features allowing to distinguish studied materials with a different chemical composition. As shown in Figure 1b, the presence of the Si−N bond in a-SiN_x results in the appearance of the PDF peak at r = 1.7 Å (A region) originally absent in the PDF pattern corresponding to a-Si. In contrast, the PDF peak at r = 2.4 Å (B region) corresponding to the presence of Si−Si bonds displayed decreased intensity compared to the same peak in PDF of a-Si. The broad peak around r = 3.0 Å is attributed to the next-nearest neighbors (C region) − beyond the bonds between the nearest neighbors and originates from the atomic arrangement in the medium range order in a-SiN_x. This peak is also characteristic for a-SiN_x structures, and its intensity depends on N concentration in the material.

Although the intensities of the peaks in simulated PDF patterns correlates with the N concentration within the materials, a presence of local highly ordered structures could also lead to a strong intensity in a simulated pattern without any particular signatures in XRD. In a SiN_x, a Si atom typically adopts fourfold coordination with the surrounding Si and N atoms, while an N atom has threefold coordination. Such bond requirement leads to −Si−N−Si−N− chain linkage in fully stoichiometric Si_3N_4 structure. However, in a substoichiometric SiN_x, due to the nitrogen deficiency, Si is primarily surrounded by other Si atoms. Therefore, the localized structures such as Si(0Si,4N) tetrahedron is unlikely to form. (Herein we define the coordination of atoms as $Si(\alpha Si,\beta N)$, where Si is the central atom of the local arrangement, α stands for the number of Si atoms bonded to the central atom, and β stands for the number of N atoms coordinated to the central atom. It should be noted that in amorphous materials the sum of α and β for Si can be below 4 due to the presence of dangling bonds.)

To evaluate the possibility of the localized crystallization (or localized ordering) within the SiN_x nanoparticle and its potential influence on the PDF pattern, we modeled locally stoichiometric-like (Si_3N_4) crystallized structures. This was performed by preparing the input configurations with the coordinate sets of 1 × 1 × 2 (28 atoms) and 2 × 2 × 3 (168 atoms) supercells denoted as Si + Si_3N_4[1 × 1 × 2] and Si + Si_3N_4[2 × 2 × 3], respectively, taking the primitive cell from Materials Project.[39] Thus, among 3067 Si and 1933 N atoms in the MD simulation supercell, we introduced 1440 Si and 1920 N atoms as 1 × 1 × 2 and 2 × 2 × 3 crystalline Si_3N_4 structures. In this initial structure preparation step, the coordinates of Si and N were set up randomly keeping only the motif local structures, mixed with the rest of Si and N to compose $SiN_{0.63}$. Then, we carried out the MD simulations for amorphous structures while we cooled from 1300 to 300 K for 40 ps by using the input configurations.

The lithiation/delithiation process proceeds through a similar pathway regardless of the content of N in the material, as was demonstrated in the earlier experimental studies.[8,13,14] Therefore, while we practiced our model to represent the experimental data for a complete range, the a-$SiN_{0.63}$ compound was studied for a baseline understanding of the conversion−alloying mechanism, as the corresponding PDF simulations could be verified experimentally.

Figure 2a represents the fraction of the first-order atomic coordination for the Si atoms in $SiN_{0.63}$ in several simulated systems: fully amorphous $SiN_{0.63}$ and $SiN_{0.63}$ with introduced localized ordering. Specifically, the systems constructed with Si_3N_4 consist of more N-rich coordination configurations for Si, such as Si(0Si,4N) and Si(1Si,3N) tetrahedrons, and Si(0Si,3N) trigonal pyramids. In contrast, in the fully amorphous $SiN_{0.63}$, the gaining entropy facilitates the preferred formation of more Si-rich coordination such as Si(3Si,1N) and Si(2Si,1N). As a result, the high fraction of N-rich Si coordination (introduced crystallinity of Si_3N_4) manifests itself in the intense PDF peak at r = 3.1 Å. Consequently, the intensity of the peak at r = 2.4 Å for Si−Si bonds lowers, as shown in the simulated PDF patterns (Figure 2b). The peak at r = 3.1 Å is attributed to the bonds between next-nearest neighbors such as Si···Si, Si···N, and N···N of Si−N−Si, Si−Si−N, and N−Si−N. The peaks at r = 1.7 and 3.1 Å are essentially associated with the presence of N in the structure; however, the simulated patterns suggest that their intensity could be not only determined by the N concentration, but also by the presence of the localized crystal structures. Furthermore, the introduced crystallinity can increase the intensities of the peaks at r =3.5 and 4.5 Å as appearing in the simulated PDF of the Si + Si_3N_4[2 × 2 × 3] system.

To further evaluate the experimental data data set and our model, we introduced hydrogen into the system. The particles of Si-based materials often may contain residual amounts of hydrogen when synthesized through the silane pyrolysis process.[40,41] Therefore, it is important to assess the influence of the hydrogen present in the structure on the PDF

https://doi.org/10.1021/acs.chemmater.2c03603
Chem. Mater. 2023, 35, 2835−2845

patterns.[42] However, our simulation confirms that incorporation of H atoms into a-$SiN_{0.63}$ structure (a-$SiN_{0.63}$:H) has no influence on the PDF pattern and thus does not lead to noticeable structural changes (such as bond distances). A similar case was observed experimentally.[43]

The simulated PDF patterns were compared to the experimentally obtained as a method for validating the modeling approach. The simulated PDF patterns with varying crystalline fragments are substantially different from the experimental PDF data, while modeling of the fully amorphous structure provides a good match to the experimental PDF pattern. The comparable PDF patterns confirm that the synthesized $SiN_{0.63}$ nanoparticles were formed fully amorphous and suggest that the simulated structure of fully amorphous $SiN_{0.63}$ well represents the synthesized $SiN_{0.63}$ nanoparticles, showing the validity from the MD to PDF simulations.

The experimental PDF analysis of battery materials is commonly performed on the materials physically removed from the electrodes. This allows performing ex situ PDF analysis at different stages of cycling.[20] The electrode layer is typically scraped from the surface of the current collector before or after electrochemical cycling, and therefore, the analyzed materials are composed of the active materials, binders, and conductive additives. The latter often corresponds to the major fraction of *inactive* components introduced in the Si-based electrodes (graphite is a common material used for such purpose, often added at the level of 15% of the total electrode mass[14]). Thus, in order to fully understand the electrochemical behavior of materials through the PDF analysis it is important to consider the presence of graphite and its influence on the PDF pattern.

Figure 3 (left panel) demonstrates the simulated PDF patterns of the composite electrode that contains graphite and

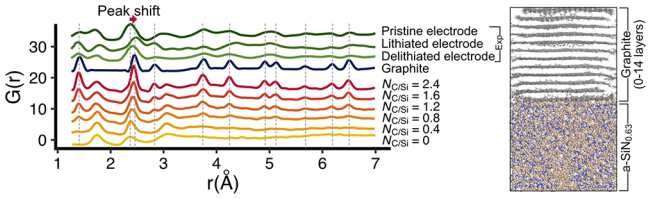

Figure 3. Experimental and simulated PDFs of a-$SiN_{0.63}$ electrodes; $N_{C/Si}$ = (Number of C atoms)/(Number of Si atoms). The scheme of an MD simulation box is illustrated in the right panel: The H-capped graphene sheets are located above the a-$SiN_{0.63}$.

a-$SiN_{0.63}$ as we varied the number of graphene layers added to the a-$SiN_{0.63}$ structure; the experimental pattern for a material taken from an electrode is also shown on top of the panel. For illustrative purposes, the ReaxFF-simulated model is demonstrated in the right panel. As expected, the increased number of graphene layers results in the growth of the graphite's peak intensity; as a result, the peak of a-$SiN_{0.63}$ at r = 2.4 Å shifts toward 2.5 Å in the PDF pattern, since the peak at r = 2.5 Å is attributed to the next-nearest C···C neighbors in graphene. Such incorporation of graphene layers allows us to closely examine the PDF changes during lithiation and delithiation processes and compare those to the results obtained experimentally.

It is worth noting that the C−C bond structure in the graphene layers is not disrupted during lithiation and delithiation processes, as Li-ions intercalate between the layers in the event of possible lithiation of graphite. Furthermore, no notable peak shift for the graphite caused by the lithiation was observed by in situ PDF analysis.[44] In the experimental PDF patterns of the lithiated electrode, the weaker PDF intensity of $SiN_{0.63}$ than that of graphite implies the bond pair loss of Si and N atoms caused by the lithiation reaction. Therefore, the PDF peak corresponding to graphite quantifies the (de)-lithiated a-SiN_x as a marker (or an internal standard) of bond pair occurrence in the PDF pattern.

In the following series of the MD simulations, we simulated the PDF patterns of an anode through the lithiation and delithiation processes. While preparing PDFs of lithiated a-$SiN_{0.63}$, we found that the lithiation reaction rate in a-$SiN_{0.63}$ drastically decreases when the lithium atoms diffused down to 13 Å below the surface in the given NVT simulation configuration (Figure S6 in the Supporting Information). As a result of partial lithiation, the simulated PDF pattern evolution halted at the intermediate stage when we used a-$SiN_{0.63}$ layer thicker than 13 Å. Furthermore, lithiation of a-$SiN_{0.63}$ is a nonequilibrium process at room temperature, where the reaction-path history is significant for the bond formation and structure determination. Therefore, the Li atoms were located only above the a-$SiN_{0.63}$ surface by the GCMC method during the simulations. Hence, to maximize the impact of lithiation on the simulated PDF within the finite MD simulation time, we inserted Li atoms above the a-$SiN_{0.63}$ region (765 Si and 482 N atoms, and 11 Å thick), while we used the hybrid GCMC/MD method. Integrating NVT (T = 300 K) MD simulations, we set the GCMC exchange rate for Li insertion at 0.6, 1, and 2 Li atoms per ps denoting then as MD-1, MD-(2,3), and MD-4, respectively. These exchange rates were selected to avoid the interactions between the adsorbed Li atoms and Li metal clusters by the rapid Li insertion. The graphite layer (1224 C atoms) was included in the simulation as discussed above. We set the cell lattice parameters with a vacuum of at least 60 Å in thickness to consider the volume expansion of a-$SiN_{0.63}$ during the lithiation. These simulations were carried out until Li metal clusters appeared above the lithiated a-$SiN_{0.63}$ as the newly inserted Li accumulated over the surface.

Through this approach, we can estimate the amount of stored Li by accounting for the lithium atoms coordinating with the Si and N atoms. Despite the different Li insertion rates in the separate MD simulations, we observed that the lithiation reaction commonly reaches a steady plateau at the amount of stored Li equivalent to the capacity of 1800 mAh/g, as shown in Figure 4a. This value is comparable to the first cycle delithiation capacity achieved experimentally in half cells.[14] Thus, $SiN_{0.63}$ structures used in this GCMC/MD simulation absorbs as much Li as in the experimental materials and, therefore, it is possible to conclude that the simulated PDF analysis should represent the experimental measurements reasonably well.

Lithiation of a-$SiN_{0.63}$ changes the local structure, and therefore, the intensity of PDF peaks at r = 1.7 and 3.1 Å lowers, as illustrated in Figure 4b. These changes result in the evolution of coordination spheres around Si and N atoms leading to different localized structures. In particular, the peak corresponding to the next-nearest neighboring pairs (r = 3.1 Å) disappeared when the amount of stored Li reached a value corresponding to a capacity of 1800 mAh/g after the MD time of about 4200 ps. This is a direct result of the Li substitution of the atoms neighboring to Si, which participates in the interactions such as Si···Si, Si···N, and N···N pairs of Si−N−

https://doi.org/10.1021/acs.chemmater.2c03603
Chem. Mater. 2023, 35, 2835−2845

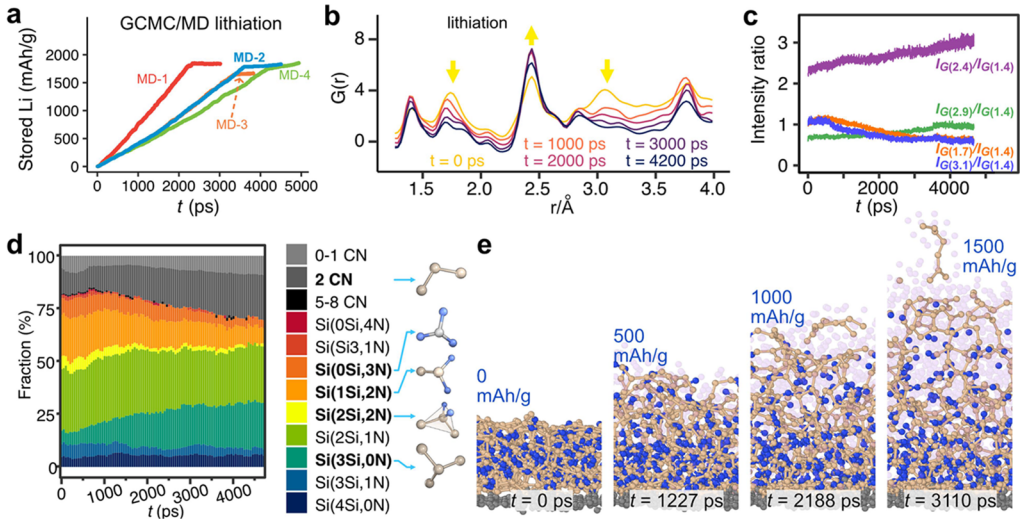

Figure 4. (a) Amount of stored Li in the separate a-$SiN_{0.63}$ grand canonical Monte Carlo and molecular dynamics (GCMC/MD) simulation trajectories, (b) simulated PDF $G(r)$ for MD-2 trajectory, and (c) intensity ratio evolution at r = 1.4, 1.7, 2.4, 2.9, and 3.1 Å as a function of MD-2 simulation time. (d) Fraction of Si-centered coordination number (CN) configurations. (e) Snapshots in the close side view. The light brown, blue, gray, and purple spheres represent Si, N, C, and Li, respectively. Only Si−Si and Si−N bonds are depicted and Li atoms are transparent for clarity; the N−N, Si−N, and Si−Si bonds are described with the bond-length cutoff of 1.2, 1.9, and 2.5 Å, respectively.

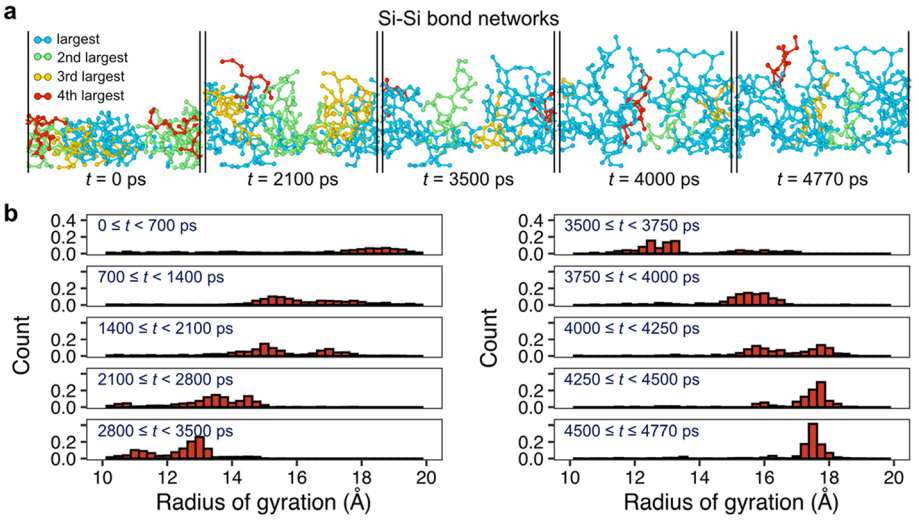

Figure 5. (a) Si−Si bond networks formed through lithiation. Only Si atoms and Si−Si bonds within lithiated a-$SiN_{0.63}$ are depicted. The cyan, green, yellow, and red spheres present the Si atoms that belong to the largest to fourth-largest network, respectively, at each snapshot. (b) Radius of gyration of the large Si−Si bond networks in lithiation.

Si, Si−Si−N, and N−Si−N bonds, respectively. The evolution of peak intensities corresponding to these interactions in comparison to the intensity of the PDF peak corresponding to C−C bonds is displayed in Figure 4c. Furthermore, the dissociation of the bond between Si and N apparently occurs during the lithiation process. As a result, the PDF peak at r = 3.1 Å diminishes and the graphite's peak at r = 2.5 Å becomes more pronounced. In contrast, the intensity increase of the peak at r = 2.4 Å suggests the different structure alteration for Si−Si, while the lithiation process breaks Si−N bonds. The increasing number of Li atoms led to the increasing ratio between the intensities corresponding to the peaks of interest and graphite, for example, for the ratio $I_{G(2.9)}/I_{G(1.4)}$ (Figure 4c). The PDF peaks corresponding to N−Li and Si−Li pairs are located at r = 1.9 and 2.7 Å, respectively (see Figure S7 in the Supporting Information). This increasing pair density may affect the peak around r = 2.4 Å due to the varying range of Si−Li distance as Li atoms move along the diffusion path. It should be noted that the lithiation process affects the PDF intensity not only by changing atomistic structure but also by the atomic number density, as $G(r)$ is computed according to eq 2. In our simulations, we accounted for the increase of X-ray scattering amplitude with a high atomic number. X-rays are less sensitive to Li atoms than N and Si, and thus, the low sensitivity of Li atoms weakens their scattering signal.[20] Therefore, the low scattering power of Li may result in a vaguely different peak change. We further examine the coordination number analysis to accurately resolve the bond formation evolution.

We investigated the coordination alteration among Si and N atoms by using R.I.N.G.S.[45] Although one can expect a coordination evolution for Li atoms as well, in this work we focused on the Si and N atoms around individual Si, because the changes in the PDF mainly correlate with their pair density.

https://doi.org/10.1021/acs.chemmater.2c03603
Chem. Mater. 2023, 35, 2835−2845

The coordination configuration analysis around the Si explains the constant Si−Si PDF intensity despite the inserted Li's chemical bond breakage in both Si−N and Si−Si bond types. As shown in Figure 4d, the decreasing fraction of N-rich configurations, such as Si(0Si,3N) and Si(1Si,2N), implies that N atoms coordinate more favorably with Li atoms. This implies that a less number of N atoms are bonded to Si as the lithiation progresses, confirming the conversion reaction as a primary mechanism of lithiation at the initial stages. The N atoms dissociated from the Si during the lithiation formed locally clustered Li_xN structures. In addition, the increasing fraction of pyramidal Si(3Si,0N)-configuration structures suggests new Si−Si bond formation. As a result, overall Si-rich configuration is dominant in the material at this stage of lithiation, which was hypothesized in the earlier studies.[14]

The structural evolution of pairs of Si−Si and Si−N is illustrated in the snapshots (Figure 4e): while the Si−N bonds dissociated with Li insertion, the Si−Si porous network adopted structurally distinct functionality to contain the inserted Li atoms. The Si atoms rearranged by forming clusters (in a form of zigzag chain) of 4−5 atoms connected together forming a pronounced Si network. Li atoms interact with these Si−Si zigzag chains through further lithiation, and a certain fraction of these Si's chains become consequently separated at high Li concentrations. As a result, the separated Si chain fragments coordinate with only Li atoms as Si−Li local structures were observed in Li_xSi structures.[19,46] As shown in the coordination configuration analysis, the increasing fraction of less-than-2-fold coordinated Si indicates more Si fragments' appearance as these Li-coordinated Si fragments remained through the lithiation reaction.

Figure 5a illustrates the snapshots with the four largest Si−Si bond networks at selected time frames. We tracked the general trends for the Si−Si coordinates and Si−Si bond networks to further examine the local rearrangements related to the Si−Si contribution in the experimental PDFs. At the beginning of Li insertion, the sizes of networks are similar to one another, being mainly separated by Si−N bonds. During the lithiation process, the largest network was dominant while the networks were connected by Si−Si.

The radius of gyration measures the effective sizes of these networks by calculating the mean-square distance from the center of the networks. The variation in the radius of gyration for these networks (Figure 5b) illustrates the analysis statistics in the Si network. This radius distribution analysis provides insights and illustrates how lithiation affected phase separation between Si-rich and N-rich phases. The Si network was formed at the start of lithiation; however, constant rearrangements essentially led to a formation of relatively large Si network, which is indicated by a large radius of gyration (close to 18 Å). Then, around t = 3500 ps, when the Li content is equivalent to the amount of stored Li under 1800 mAh/g, Si formed a dominant network and the radius of gyration decreased to about 13 Å despite the volume expansion of lithiated $SiN_{0.63}$. At later simulation times, the high population of sizes corresponding to Si-based networks at 17.5 Å indicates the stable network formation.

Therefore, during the lithiation process, as Li takes the place of N sites breaking Si−N bonds (conversion reaction), the Si-rich chains were clearly formed. In addition, the Li atoms participated in isolation of some Si and N atoms by breaking the Si−Si and Si−N bonds. This structure rearrangement resulted in Si's steady CN through the lithiation process. In the experimental PDF for the lithiated anode, it is worth noting that the weaker PDF intensity at r = 2.4 Å suggests that the isolated Si atoms became more prevalent. Furthermore, this PDF peak intensity at r = 2.4 Å also should be weaker as the Si-network underwent lithiation (alloying reaction).

The delithiation behavior is also critical for the understating of the conversion−alloying mechanism as well as for understanding of the changes in PDF. For a number of CAMs, it is still unclear what kind of structures are formed through the first cycle, which includes lithiation and subsequent delithiation. Thus, we investigated the series of structural changes occurring through the delithiation process by starting with lithiated structures merged with graphite (graphene layers). To examine the delithiated a-$SiN_{0.63}$ structure, we presumed that Li atoms at the a-SiN_x surface were removed during the first cycle. While we removed the randomly selected Li atoms within a distance of 6 Å from the a-$SiN_{0.63}$ surface at every 100 ps in the NTV (T = 300 K) MD simulations, the repeated gradient of Li concentration in MD simulation led to the delithiated material. Furthermore, the delithiation process was initiated when the amount of stored Li was equivalent to the capacity of 1714 mAh/g (1780 Li atoms). Because the excessive Li atoms started forming the Li metal layer above the lithiated a-$SiN_{0.63}$, and the spurious structural deformation was subsequently induced by the inserted Li atoms within the layer when the amount of stored Li is over 1840 mAh/g by the GCMC/MD simulations, we circumvented either possible phase separation or irregular bond formation by conducting the delithiation process below the fully lithiated state. Hence, we could compare the lithiation and delithiation processes by isolating the role of the structure alteration mechanism induced by the excessive number of Li atoms. A series of MD simulations were conducted until we found no Li atoms above the surface. When we finished a series of delithiation simulation, there were 172 Li atoms left below the surface.

The amount of stored Li as a function of simulation time and PDFs corresponding to the structures formed during delithiation is shown in Figure 6a. The simulated PDF

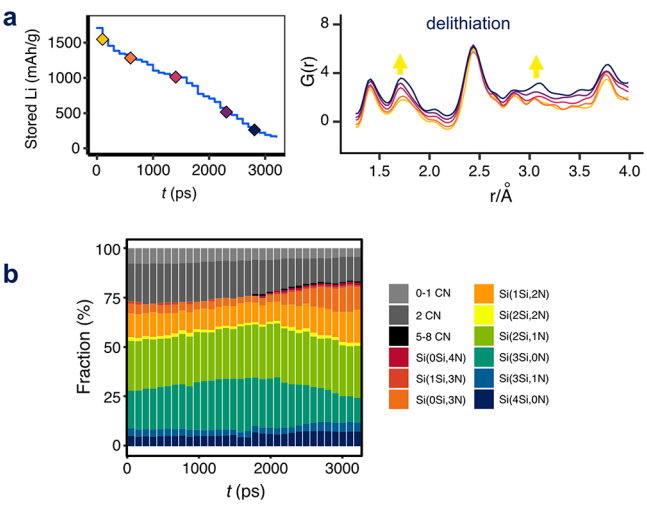

Figure 6. (a) Amount-of-stored-Li of a-$SiN_{0.63}$ and the simulated PDFs during delithiation. The values of the amount of stored Li for the presented PDFs (right panel) are marked by the corresponding color diamonds (left panel). (b) Fraction of coordination configurations around Si.

https://doi.org/10.1021/acs.chemmater.2c03603
Chem. Mater. 2023, 35, 2835−2845

illustrates that the peaks at r = 1.7 and 3.1 Å are restored as the Si−N bonds are reformed after Li removal. Compared to the graphite peaks, the peaks for the Si−N distance and its next-nearest neighbor distance reinstated as strong as the pristine a-$SiN_{0.63}$. The fraction change of Si's coordination configuration demonstrated this reformation progress for the Si−Si and Si−N bonds, as shown in Figure 6b.

The decrease of less-than-2 CN shows that the Si- and N-atom fragments form either a Si−Si or Si−N bond. As the delithiation progressed, the fragments reformed the bonds with the other available atoms at the adjacent Li-vacancy sites. A change in delithiation behavior is clearly notable at around the MD 2000 ps time, which concerns three- and fourfold coordination configurations. Up to 2000 ps, the increasing fraction of Si-rich configurations suggests that the formation of a Si−Si bond network is more favorable over the formation of Si−N bonds as Li atoms were removed from the structure. It is the most distinctive through the analysis of the Si(3Si,0N) configuration, whose fraction steadily increases. This trend also showed that N atoms coordinated with Li kept such coordination more strongly than Si, as N−Li dissociation occurs at a lower rate than Si−Li dissociation. The constant fraction of N-rich fragments through delithiation implies less bonding reformation between Si and N atoms, while the N−Li bonds hamper the Si−N formations at a certain level of stored Li's. This N−Li rich region may function as a preformed passivation layer in the materials through the cycling, similar to the formation of matrix in the materials characterized experimentally.

However, from 2000 ps, an increasing fraction of N-rich configurations becomes notable, while the relative fraction of the Si-rich configuration decreases. As the Li atoms left the Si- and N-coordinated sites due to the Li concentration gradient, there are no adjacent Li atoms around the remaining Si and N atoms. This further leads to Si−N and −Si−N-Si−N− chain network formation similar to the one found in Si_3N_4. Therefore, the bond formation pathways of these atoms undergo to the most favorable geometric network in free energy. As a result, Si's N-rich configuration reformation lowers the free energy, competing for the phase separation of the Si and N atoms. This binary Si nitride phase is stable while the Si and N atoms reform Si−N bonds as the N-rich configuration, such as Si(1Si,3N) and Si(0Si,3N).

It should be noted that we removed the Li atoms until we could not find any Li atoms below the surface. When the amount of the stored Li was equivalent to a gravimetric capacity of 163 mAh/g, no Li atoms diffused over the surface despite the Li concentration gradient, an observation similar to the experimental systems. The experimental PDF of the delithiated electrode showed that the intensities of the peaks corresponding to Si−N are not fully recovered, probably due to the irreversible reactions, which involved trapping of Li atoms inside the particle. This may also cause a hysteresis in the structural reorganization during the lithiation and delithiation cycles. Thus, we have made an attempt to compare the structures formed in the process of lithiation and delithiation to understand the possible chemical nature of the hysteresis.

As we observed the growth of Si−Si network during the lithiation progression, we also found that the Si−Si network evolved during the delithiation step as well. During this process, Li atoms continuously participated in the formation and breaking of the Si−Li bond during Li's diffusion, as a result changing the local and long-range arrangements of Si atoms. Similar to the analysis of lithiated structures, the radius of gyration of the Si network is shown in Figure 7. The Si−Si

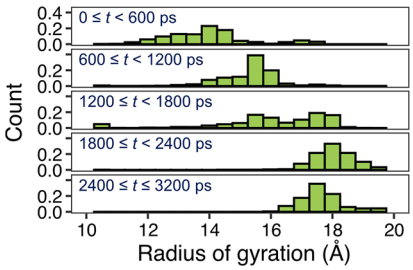

Figure 7. Radius of gyration of the large Si−Si bond networks in delithiation.

network expanded even though the volume of lithiated $SiN_{0.63}$ decreased during the delithiation process. The trend of the radius of gyration was reversed when the amount of stored Li was less than 500 mAh/g ($2400 \leq t \leq 3200$ ps) due to the volume shrinkage. Thus, both lithiation and delithiation processes play a crucial role in the Si−Si network formation.

The analysis of both lithiation and delithiation processes showed that Si−Si formation is favored over Si−N formation. Figure 8 displays the evolution of the averaged coordination

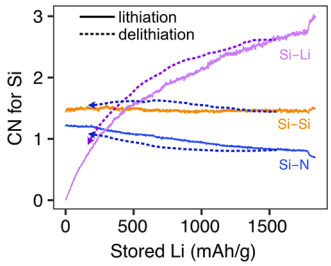

Figure 8. Si's average coordination number with Li, Si, and N in the lithiation and delithiation processes.

number for the Si atoms with the surrounding atoms to demonstrate the changes in the coordination configuration of the Si phases during the first cycle. In the lithiation process, only Si−N pair densities decrease, while the Si−Si CN is almost constant within the simulation time. This is due to the formation of new Si−Si bonds, as the lithiation process led to not only the dissociation of existing Si−Si bonds but also to formation of new ones. The CN analysis of the delithiation process showed that Si−Si formation was also favored over Si−N formation during the delithiation. The averaged CN for Si increased when the delithiation process was initiated. This increase contrasted with the lithiation process, where the Si−Si coordination number is almost constant, implying that the Si−Si bonds formation increased during the delithiation. The coordination number of Si−N is steady until the Si's N-rich configuration increases again with the amount of stored Li under 800 mAh/g. This trend suggests different rates of Si−Si and Si−N bond reformation in response to the amount of the stored Li. This restoration behavior in the Si and N bond network results in the different structures between lithiation and delithiation during each process, as it was observed in the experimental PDFs.

We also analyzed the local Si−Li coordination in a-$SiN_{0.63}$ during lithiation and delithiation by investigating the depend-

https://doi.org/10.1021/acs.chemmater.2c03603
Chem. Mater. 2023, 35, 2835−2845

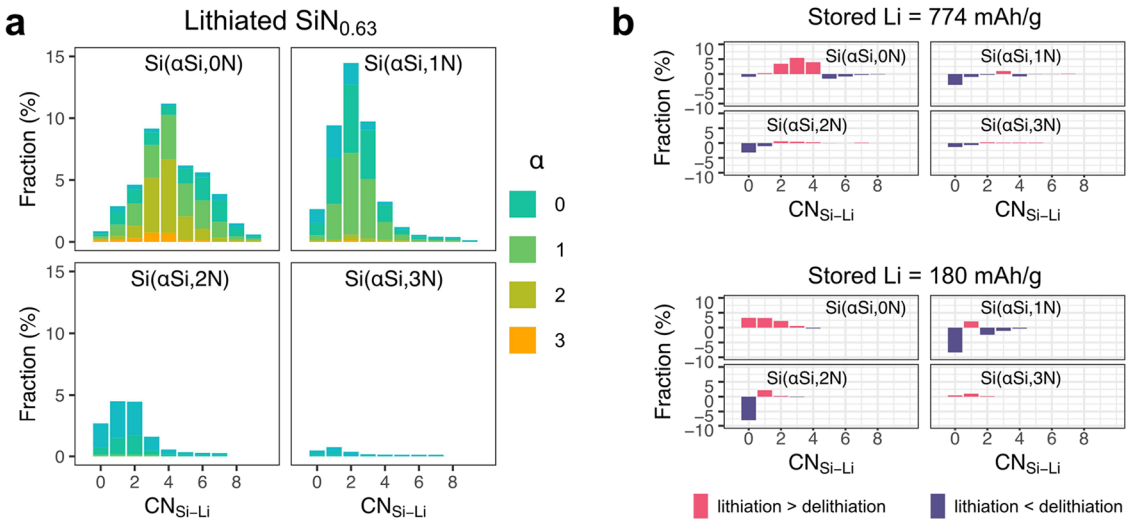

Figure 9. (a) CN between Si and Li at the amount of stored Li equivalent to capacity of 1840 mAh/g. (b) Coordination number differences between the lithiation and delithiation processes.

ency of the coordination number on the number of Si−N bonds around a centered Si atom. Through the CN analysis, we assessed the number of Si−Li bonds for each Si atom in the trajectories. Such assessment for lithiated a-$SiN_{0.63}$, with the amount of stored Li is 1840 mAh/g, is presented in Figure 9a. Expectantly, we found no Si−Li coordination for the Si atom in the case of Si(4Si,0N) and Si(0Si,4N) configurations (tetrahedron).

This analysis shows that more Li atoms are located around Si, when a Si atom is not bonded to any N atoms leading to fourfold Si−Li coordination (Figure 9a, top-left panel). Moreover, its Si−Li CN distribution shows that the pure Si-bond network can afford high Li concentration. In contrast, when a Si atom coordinates with N (top-right panel), the fraction of fourfold Si−Li coordinations drops drastically as the most probable CN is two. These CN distributions support the previously hypothesized lithiation pathways. The lithiated a-SiN_x compositions include the mixtures of stable binary Li−Si and ternary Li−Si−N compounds in lithiation.[13,14]

We found some distributions change for the Si−Li CN inside the structure by comparing the Si−Li CN distribution through the analysis of lithiation and delithiation processes despite the same Li concentration (Figure 9b). Li atom locates favorably around the pure Si region in the lithiation process. Meanwhile, Li leaves the Si site favorably that coordinates with N in the delithiation process as there are more Si atoms with CN_{Si-Li} = 0 (negative value in difference). Intriguingly, it is notable that the Si atoms bonded to N better release Li during delithiation. The change is insignificant as we observed the Si−N network restoration despite the Si networking induced by Li diffusion. This restoration feature of SiN_x may explain the cycling stability of the material.

Finally, for the future experimental verification, we compared the PDFs of lithiated a-$SiN_{0.63}$ compounds with the equivalent Li concentrations. As shown in Figure 10, the PDFs display similar patterns despite some structural differences described above.

Although we observed the Si-network formation during the lithiation and delithiation, Si−N reformation was also promoted by Li removal. However, this observation of similarities was unexpected because the experimental PDF of the delithiated anode showed a low intensity at r = 3.1 Å. We

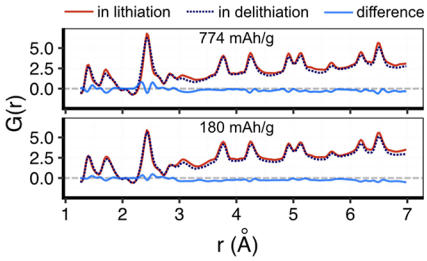

Figure 10. Comparisons of the simulated G(r) of a-$SiN_{0.63}$ at the same amount of stored Li but between in lithiation and delithiation processes.

speculate that the weaker intensity resulted from the lowered density of the SiN_x material by the solid electrolyte interphase (SEI) formation while the experiments were conducted. Meanwhile, this work's MD and PDF simulations display only the difference in the void created during the delithiation process. As the broadly weakened intensity around r = 1.7 and 3.1 Å indicated in the simulated PDF, the Si−N and next-nearest Si···N pair changes are reflected in the difference.

4. CONCLUSIONS

In summary, we developed an effective and practical approach to investigate the atomistic structure evolution of materials that undergo a conversion−alloying process in batteries using a Si-based active material for LIBs as a model system. The reactive molecular dynamics were coupled with the PDF simulation to complement the experimental measurements. The experimental PDF was used for the verification of the modeling results.

Subsequently, this approach was used to understand the cycling stability of substoichiometric a-SiN_x anode materials by revealing the atomistic features relevant to the changes this material undergoes during lithiation and delithiation processes in a LIB. In the lithiation process, Li replacement with N is predominant (conversion reaction) over the formation of lithiated Si (alloying reaction), while some of Si atoms formed chain-shape fragments through a lithiation process. In a fully lithiated a-SiN_x, the Li atoms are predominantly located around the pure-Si bond sites compared to the Si atoms bonded to N. Hence, the coordination analysis illustrates the

https://doi.org/10.1021/acs.chemmater.2c03603
Chem. Mater. 2023, 35, 2835−2845

composition, where there are the mixtures of stable binary Li−Si and ternary Li−Si−N compounds formed through the lithiation.

During delithiation of a-SiN_x, the Si−N bond reformation is promoted because of low Li concentration. Meanwhile, Si−Si reformation was generally favored over Si−N reformation. Consequently, despite the structures' hysteresis, further delithiation led to increasing Si−N pair reformation until as Li concentration low as in the stable Li−Si−N ternary compound was achieved. Overall, we expect that the use of the proposed approach will allow to comprehensively understand not only lithiation and delithiation mechanisms in the studied materials, but also the multicomponent phase transformation in other amorphous materials for batteries.

■ ASSOCIATED CONTENT

Supporting Information

The Supporting Information is available free of charge at https://pubs.acs.org/doi/10.1021/acs.chemmater.2c03603.

ReaxFF force field parameters; force field validation; comparison of graphene structure and the simulated PDF; snapshots and PDF of lithiated and delithiated $SiN_{0.63}$ (PDF)

$SiN_{0.63}$ in the lithiation at 300 K (MP4)

■ AUTHOR INFORMATION

Corresponding Authors

Heesoo Park − *Centre for Material Science and Nanotechnology, Department of Chemistry, University of Oslo, 0371 Oslo, Norway;* orcid.org/0000-0002-4276-6843; Email: heesoo.park@smn.uio.no

Alexey Y. Koposov − *Centre for Material Science and Nanotechnology, Department of Chemistry, University of Oslo, 0371 Oslo, Norway; Department of Battery Technology, Institute for Energy Technology (IFE), 2027 Kjeller, Norway;* orcid.org/0000-0001-5898-3204; Email: alexey.koposov@kjemi.uio.no

Author

Adri C. T. van Duin − *Department of Mechanical Engineering, The Pennsylvania State University, University Park, Pennsylvania 16802, United States;* orcid.org/0000-0002-3478-4945

Complete contact information is available at: https://pubs.acs.org/10.1021/acs.chemmater.2c03603

Notes

The authors declare no competing financial interest.

■ ACKNOWLEDGMENTS

This work was performed with the support of MoZEES, a Norwegian Centre for Environment-friendly Energy Research (FME), co-sponsored by the Research Council of Norway (project number 257653). The authors acknowledge the Research Council of Norway for providing the computer time (under the project numbers NN2875k and NS2875k) at the Norwegian supercomputer facility.

■ REFERENCES

(1) Duduta, M.; Rivaz, S.; Clarke, D. R.; Wood, R. J. Ultra-Lightweight, High Power Density Lithium-Ion Batteries. *Batteries Supercaps* **2018**, *1*, 131−134.

(2) Ji, K.; Han, J.; Hirata, A.; Fujita, T.; Shen, Y.; Ning, S.; Liu, P.; Kashani, H.; Tian, Y.; Ito, Y.; Fujita, J.-I.; Oyama, Y. Lithium intercalation into bilayer graphene. *Nat. Commun.* **2019**, *10*, 275.

(3) Zhao, L. F.; Hu, Z.; Lai, W. H.; Tao, Y.; Peng, J.; Miao, Z. C.; Wang, Y. X.; Chou, S. L.; Liu, H. K.; Dou, S. X. Hard Carbon Anodes: Fundamental Understanding and Commercial Perspectives for Na-Ion Batteries beyond Li-Ion and K-Ion Counterparts. *Adv. Energy Mater.* **2021**, *11*, No. 2002704.

(4) Obrovac, M. N.; Chevrier, V. L. Alloy Negative Electrodes for Li-Ion Batteries. *Chem. Rev.* **2014**, *114*, 11444−11502.

(5) Bresser, D.; Passerini, S.; Scrosati, B. Leveraging valuable synergies by combining alloying and conversion for lithium-ion anodes. *Energy Environ. Sci.* **2016**, *9*, 3348−3367.

(6) Larcher, D.; Beattie, S.; Morcrette, M.; Edström, K.; Jumas, J.-C.; Tarascon, J.-M. Recent findings and prospects in the field of pure metals as negative electrodes for Li-ion batteries. *J. Mater. Chem.* **2007**, *17*, 3759−3772.

(7) Yim, C.-H.; Courtel, F. M.; Abu-Lebdeh, Y. A high capacity silicon−graphite composite as anode for lithium-ion batteries using low content amorphous silicon and compatible binders. *J. Mater. Chem. A* **2013**, *1*, 8234−8243.

(8) Suzuki, N.; Cervera, R. B.; Ohnishi, T.; Takada, K. Silicon nitride thin film electrode for lithium-ion batteries. *J. Power Sources* **2013**, *231*, 186−189.

(9) Fang, L.; Bahlawane, N.; Sun, W.; Pan, H.; Xu, B. B.; Yan, M.; Jiang, Y. Conversion-Alloying Anode Materials for Sodium Ion Batteries. *Small* **2021**, *17*, No. 2101137.

(10) Skurtveit, A.; Brennhagen, A.; Park, H.; Cavallo, C.; Koposov, A. Y. Benefits and Development Challenges for Conversion-Alloying Anode Materials in Na-Ion Batteries. *Front. Energy Res.* **2022**, *10*, No. 897755.

(11) Obrovac, M. N.; Christensen, L.; Le, D. B.; Dahn, J. R. Alloy Design for Lithium-Ion Battery Anodes. *J. Electrochem. Soc.* **2007**, *154*, A849.

(12) Uxa, D.; Jerliu, B.; Hüger, E.; Dörrer, L.; Horisberger, M.; Stahn, J.; Schmidt, H. On the Lithiation Mechanism of Amorphous Silicon Electrodes in Li-Ion Batteries. *J. Phys. Chem. C* **2019**, *123*, 22027−22039.

(13) Ulvestad, A.; Mæhlen, J. P.; Kirkengen, M. Silicon nitride as anode material for Li-ion batteries: Understanding the SiNx conversion reaction. *J. Power Sources* **2018**, *399*, 414−421.

(14) Ulvestad, A.; Skare, M. O.; Foss, C. E.; Krogsæter, H.; Reichstein, J. F.; Preston, T. J.; Mæhlen, J. P.; Andersen, H. F.; Koposov, A. Y. Stoichiometry-Controlled Reversible Lithiation Capacity in Nanostructu red Silicon Nitrides Enabled by in Situ Conversion Reaction. *ACS Nano* **2021**, *15*, 16777−16787.

(15) Billinge, S. J. L. The rise of the X-ray atomic pair distribution function method: a series of fortunate events. *Philos. Trans. R. Soc. A* **2019**, *377*, No. 20180413.

(16) Christiansen, T. L.; Cooper, S. R.; Jensen, K. M. Ø. There's no place like real-space: elucidating size-dependent atomic structure of nanomaterials using pair distribution function analysis. *Nanoscale Adv.* **2020**, *2*, 2234−2254.

(17) Ostadhossein, A.; Cubuk, E. D.; Tritsaris, G. A.; Kaxiras, E.; Zhang, S.; Duin, A. C. T. Stress effects on the initial lithiation of crystalline silicon nanowi res: reactive molecular dynamics simulations using ReaxFF. *Phys. Chem. Chem. Phys.* **2015**, *17*, 3832−3840.

(18) Basu, S.; Koratkar, N.; Shi, Y. Structural transformation and embrittlement during lithiation and delithiation cycles in an amorphous silicon electrode. *Acta Mater.* **2019**, *175*, 11−20.

(19) Chan, M. K. Y.; Wolverton, C.; Greeley, J. P. First Principles Simulations of the Electrochemical Lithiation and Delithiation of Faceted Crystalline Silicon. *J. Am. Chem. Soc.* **2012**, *134*, 14362−14374.

(20) Key, B.; Morcrette, M.; Tarascon, J.-M.; Grey, C. P. Pair Distribution Function Analysis and Solid State NMR Studies of Sil icon Electrodes for Lithium Ion Batteries: Understanding the (De)lithiation Mechanisms. *J. Am. Chem. Soc.* **2011**, *133*, 503−512.

(21) Zhang, W.; van Duin, A. C. T. Atomistic-Scale Simulations of the Graphene Growth on a Silicon Carbide Substrate Using Thermal Decomposition and Chemical Vapor Deposition. *Chem. Mater.* **2020**, *32*, 8306−8317.
(22) Muraleedharan, M. G.; Asgar, H.; Mohammed, S.; Gadikota, G.; van Duin, A. C. T. Elucidating Thermally Induced Structural and Chemical Transformations in Kaolinite Using Reactive Molecular Dynamics Simulations and X-ray Scattering Measurements. *Chem. Mater.* **2020**, *32*, 651−662.
(23) Russo, M. F.; van Duin, A. C. T. Atomistic-scale simulations of chemical reactions: Bridging from quantum chemistry to engineering. *Nucl. Instrum. Methods Phys. Res., Sect. B* **2011**, *269*, 1549−1554.
(24) Kresse, G.; Furthmüller, J. Efficient iterative schemes for ab initio total-energy calculations using a plane-wave basis set. *Phys. Rev. B* **1996**, *54*, 11169−11186.
(25) Kresse, G.; Furthmüller, J. Efficiency of ab-initio total energy calculations for metals and semiconductors using a plane-wave basis set. *Comput. Mater. Sci.* **1996**, *6*, 15−50.
(26) Kresse, G.; Hafner, J. Ab initio molecular dynamics for liquid metals. *Phys. Rev. B* **1993**, *47*, 558−561.
(27) Neese, F. Software update: The ORCA program system—Version 5.0. *WIREs Comput. Mol. Sci.* **2022**, *12*, No. e1606.
(28) Neese, F. The ORCA program system. *WIREs Comput. Mol. Sci.* **2012**, *2*, 73−78.
(29) Aktulga, H. M.; Fogarty, J. C.; Pandit, S. A.; Grama, A. Y. Parallel reactive molecular dynamics: Numerical methods and algorithmic techniques. *Parallel Comput.* **2012**, *38*, 245−259.
(30) Thompson, A. P.; Aktulga, H. M.; Berger, R.; Bolintineanu, D. S.; Brown, W. M.; Crozier, P. S.; Veld, P. J.; Kohlmeyer, A.; Moore, S. G.; Nguyen, T. D.; Shan, R.; Stevens, M. J.; Tranchida, J.; Trott, C.; Plimpton, S. J. LAMMPS − a flexible simulation tool for particle-based materials modeling at the atomic, meso, and continuum scales. *Comput. Phys. Commun.* **2022**, *271*, No. 108171.
(31) Stukowski, A. Visualization and analysis of atomistic simulation data with OVITO−the Open Visualization Tool. *Modell. Simul. Mater. Sci. Eng.* **2010**, *18*, No. 015012.
(32) Neverov, V. S. XaNSoNS: GPU-accelerated simulator of diffraction patterns of nanoparticles. *SoftwareX* **2017**, *6*, 63−68.
(33) Farrow, C. L.; Juhas, P.; Liu, J. W.; Bryndin, D.; Božin, E. S.; Bloch, J.; Proffen, T.; Billinge, S. J. L. PDFfit2 and PDFgui: computer programs for studying nanostructure in crystals. *J. Phys.: Condens. Matter* **2007**, *19*, No. 335219.
(34) Wang, X.; Tan, S.; Yang, X.-Q.; Hu, E. Pair distribution function analysis: Fundamentals and application to battery materials. *Chin. Phys. B* **2020**, *29*, No. 028802.
(35) Housel, L. M.; Li, W.; Quilty, C. D.; Vila, M. N.; Wang, L.; Tang, C. R.; Bock, D. C.; Wu, Q.; Tong, X.; Head, A. R.; Takeuchi, K. J.; Marschilok, A. C.; Takeuchi, E. S. Insights into Reactivity of Silicon Negative Electrodes: Analysis Using Isothermal Microcalorimetry. *ACS Appl. Mater. Interfaces* **2019**, *11*, 37567−37577.
(36) Yen, B. K.; White, R. L.; Waltman, R. J.; Dai, Q.; Miller, D. C.; Kellock, A. J.; Marchon, B.; Kasai, P. H.; Toney, M. F.; York, B. R.; Deng, H.; Xiao, Q.-F.; Raman, V. Microstructure and properties of ultrathin amorphous silicon nitride protective coating. *J. Vac. Sci. Technol.* **2003**, *21*, 1895−1904.
(37) Hintzsche, L. E.; Fang, C. M.; Watts, T.; Marsman, M.; Jordan, G.; Lamers, M. W. P. E.; Weeber, A. W.; Kresse, G. Density functional theory study of the structural and electronic properties of amorphous silicon nitrides: Si_3N_{4-x}:H. *Phys. Rev. B* **2012**, *86*, No. 235204.
(38) Martínez, L.; Andrade, R.; Birgin, E. G.; Martínez, J. M. PACKMOL: A package for building initial configurations for molecular dynamics simulations. *J. Comput. Chem.* **2009**, *30*, 2157−2164.
(39) Jain, A.; Ong, S. P.; Hautier, G.; Chen, W.; Richards, W. D.; Dacek, S.; Cholia, S.; Gunter, D.; Skinner, D.; Ceder, G.; Persson, K. A. Commentary: The Materials Project: A materials genome approach to accelerating materials innovation. *APL Mater.* **2013**, *1*, No. 011002.
(40) Liu, S.-S.; Li, H.; Xiao, W.-D. Sintering effect on crystallite size, hydrogen bond structure and morphology of the silane-derived silicon powders. *Powder Technol.* **2015**, *273*, 40−46.
(41) Wiggers, H.; Starke, R.; Roth, P. Silicon Particle Formation by Pyrolysis of Silane in a Hot Wall Gasphase Reactor. *Chem. Eng. Technol.* **2001**, *24*, 261−264.
(42) Ulvestad, A.; Reksten, A. H.; Andersen, H. F.; Carvalho, P. A.; Jensen, I. J. T.; Nagell, M. U.; Mæhlen, J. P.; Kirkengen, M.; Koposov, A. Y. Crystallinity of Silicon Nanoparticles: Direct Influence on the Electrochemical Performance of Lithium Ion Battery Anodes. *ChemElectroChem* **2020**, *7*, 4349−4353.
(43) Gritsenko, V. A.; Kruchinin, V. N.; Prosvirin, I. P.; Novikov, Y. N.; Chin, A.; Volodin, V. A. Atomic and Electronic Structures of a-SiNx:H. *J. Exp. Theor. Phys.* **2019**, *129*, 924−934.
(44) Liu, X.; Yin, L.; Ren, D.; Wang, L.; Ren, Y.; Xu, W.; Lapidus, S.; Wang, H.; He, X.; Chen, Z.; Xu, G.-L.; Ouyang, M.; Amine, K. In situ observation of thermal-driven degradation and safety concerns of lithiated graphite anode. *Nat. Commun.* **2021**, *12*, 4235.
(45) Le Roux, S.; Jund, P. Ring statistics analysis of topological networks: New approach and application to amorphous GeS2 and SiO2 systems. *Comput. Mater. Sci.* **2010**, *49*, 70−83.
(46) Cho, Y.-H.; Booh, S.; Cho, E.; Lee, H.; Shin, J. Theoretical prediction of fracture conditions for delithiation in silicon anode of lithium ion battery. *APL Mater.* **2017**, *5*, 106101.

https://doi.org/10.1021/acs.chemmater.2c03603
Chem. Mater. 2023, 35, 2835−2845